Wettability of carbon nanotube-grafted carbon fibers and their interfacial properties in polypropylene thermoplastic composite

Jian Wang,[a,b,c*] David B Anthony,[d] Carlos A Fuentes,[c,g] Hugo G De Luca,[e] Dongxing Zhang,[b] Alexander Bismarck,[f] Aart Willem Van Vuure,[c] Milo SP Shaffer,[d,e] David Seveno[c†]

a) Industrial Research Institute of Nonwovens & Technical Textiles, College of Textiles & Clothing, Qingdao University, Qingdao 266071, China
b) School of Materials Science and Engineering, Harbin Institute of Technology, Harbin 150001, China
c) Department of Materials Engineering, KU Leuven, Kasteelpark Arenberg, 44 B-3001 Leuven, Belgium
d) Department of Chemistry, Imperial College London, 80 Wood Lane, London W12 0BZ, UK
e) London Centre for Nanotechnology, Department of Materials, Imperial College London, South Kensington Campus, London SW7 2AZ, UK
f) Faculty of Chemistry, Institute of Materials Chemistry, Polymer & Composite Engineering (PaCE) Group, University of Vienna, Währinger Str. 42, A-1090 Vienna, Austria
g) Materials Research and Technology Department, Luxembourg Institute of Science and Technology, L-4940 Hautcharage, Luxembourg

Corresponding authors

* jianwang@qdu.edu.cn
† david.seveno@kuleuven.be

Abstract

The interfacial properties of carbon fiber (CF) reinforced thermoplastic composites depend strongly on the wettability and surface characteristics of the reinforcing fibers, and their compatibility with a chosen matrix. The interface between conventional fibers and thermoplastic matrices is generally weak, due to a lack of specific chemical interaction, especially in the case of polyolefins. Carbon nanotube-grafted-carbon fibers (CNT-g-CF) are considered to be potential reinforcements as they provide additional mechanical interlocking. Commercial CFs were successfully grafted with nanotubes using a continuous, and hence scalable, CVD method. X-ray photoelectron spectroscopy, Wilhelmy wetting measurements, and scanning electron microscopy confirmed the successful grafting and resulting hydrophobic surface chemistry, dominated by van der Waals interactions. The grafted CNTs, with diameters and lengths around 10 nm and 140 nm respectively, were well suited to improve the overall wettability and interfacial shear

strength (+53.4%) of the CNT-g-CF in a polypropylene matrix when compared to as-received unsized CFs.

Keywords

Carbon fibers; Carbon nanotubes; Wettability; Thermoplastic composites;

1 Introduction

Carbon fiber (CF) reinforced thermoplastic composites (CFRTPs) are now used in a variety of high-performance structural applications for their excellent properties such as high specific stiffness and strength, outstanding toughness, short mold cycle times and recyclability [1,2]. Composite interfaces are pivotal for the integrity and performance of the material, acting as the connection between the matrices and reinforcements for stress transfer [3–5]. However, the combination of smooth, inert fibers, with unreactive thermoplastic matrices often produces weak interfaces that limit the ultimate mechanical performance of the composite. In thermoset systems, partial oxidation of the surface activates chemical reactions between the CFs and the polymer matrices (or sizing) [6]. In non-reactive thermoplastic systems, both wetting and adhesion may be inadequate, leading to weak compression and interlaminar properties [7]. The problem is especially acute in cheap, otherwise attractive polyolefins, such as polypropylene, which have no functional groups and low polarity [8–10]. There is, therefore, a large amount of research focusing on the manipulation of CF surfaces, aiming to improve the fiber/matrix interfaces in CFRTPs. Methods commonly used include fiber coating [11–13], oxidation treatments [14] and surface grafting [15].

Aggressive chemical/plasma treatments or high temperature processes alter surface chemistry but can damage CF surface, negatively affecting their mechanical properties. Additionally, functional groups introduced on CF surfaces have poor chemical compatibility with thermoplastic matrices without matrix

modifications, resulting only in marginal improvements of the interfacial/interphase properties. Whilst, there is a growing body of literature that recognizes grafting carbon nanotubes (CNTs) onto the surface of CFs to generate hierarchical CNT-grafted fiber composites is an valid approach to enhance the interfacial shear strengths in thermosetting systems [15–19]. Recently, a continuous roll-to-roll thermal chemical vapor deposition (CVD) method has been reported to prepare carbon nanotube-grafted-carbon fibers (CNT-g-CFs), which exhibit higher interfacial shear strengths (IFSS) with epoxy resins as compared to both unsized and commercially sized carbon fibers [20,21]. Typically, grafting CNTs onto CFs is thought to improve the IFSS by mechanical keying (ineterlocking) for effective load transfer [17,22,23]. Model single fiber composite tests are routinely used to rank interfacial properties (IFSS), which may indicate future performance in composite laminates [24–26]. However, the majority of related studies focus on the interfacial properties of CNT-g-CFs with thermosetting resins, particularly epoxy [20,27,28]. Reports on IFSS of CNT-g-CFs reinforced thermoplastic composites are so far very limited [16,19,29].

The wettability of the fibers by the matrix is an important aspect of determining interfacial properties, especially for CFRTPs [30]. To consider the physical interactions between fiber and matrix quantitatively, the fibre surface energy is typically determined from measured contact angles, for example using the well-established Wilhelmy method [31–34]. The surface energy of a solid or liquid can be divided into various components, i.e., the Lifshitz-van der Waals, acid and base components [35]. These components represent the physical and wetting properties of liquids and solids, and can be used to predict the thermodynamic work of adhesion between fibers and polymer matrices [7,36,37]. Previous studies [38,39] have also tried to establish a link between the work of adhesion and “practical” adhesion at the single fiber scale. Whilst there are a few reports relating conventional fiber wettability to interfacial mechanical properties [7,27,37,40–42], similar studies for CNT-g-CFs are almost entirely lacking [16].

In the present study, CNT-g-CFs were prepared by a continuous CVD approach that may be scaled to larger scale production in the future. The Wilhelmy method was applied to measure the dynamic contact angles between individual (CNT-g-)CFs and different probe liquids. The CF surface energy components were then determined by using the acid-base approach [43] so that the thermodynamic work of adhesion between these modified CFs and thermoplastic resin, polypropylene, could be predicted. In addition, the morphology and chemical characteristics of the CF surfaces were investigated using scanning electron microscopy (SEM) and X-ray photoelectron spectroscopy (XPS), respectively. Microdroplet debond tests were performed to determine the IFSS between these CFs and a PP matrix at the single fiber scale, in order to validate the predictions and evaluate the potential use of CNTs to enhance CF-PP composites.

2 Experimental

2.1 Materials

Polyacrylonitrile (PAN)-based commercially sized carbon fibers with a ~ 1 wt.% sizing developed for epoxy systems (AS4C-GP-12K-8, datasheet diameter 6.9 μm, hereafter referred to as sized CFs) and unsized PAN-based carbon fibers (AS4-12K-7D, datasheet diameter 7.1 μm, hereafter referred to as unsized CFs) were kindly provided by Hexcel Composites (Duxford, GB). Nickel(II) acetylacetonate (≥98%, VWR, GB), iron(III) nitrate nonahydrate (≥98%, Sigma-Aldrich, GB) and ethanol (>99.7%, VWR, GB) were procured to prepare the catalyst precursor loaded sized carbon fibers substrate for CNT synthesis. Isotactic polypropylene (515A, Sabic, D, hereafter referred to as PP) was used for microdroplet tests.

2.2 Synthesis of carbon nanotube-grafted carbon fibers

CNT-g-CFs were manufactured using a continuous and open CVD reactor developed at Imperial College London, and the detaild synthesis parameters were described in previous paper [20]. In brief, the

growth of CNTs on CFs was performed on sized carbon fibers, as-received without prior treatment/processing, which were pre-deposited with bi-catalyst precursor prior to synthesis, 12k tow (iron and nickel salts). The CNT synthesis was carried out with an applied potential difference (300 V) between the fibers and a cylindrical coaxial graphite foil counter electrode. In the stable hot zone of the reactor (770 °C) the catalyst is reduced (5 min) by a hydrogen (2.4 vol.%) in nitrogen (97.6 vol.%) premix and subsequently acetylene (1.3 vol.%) in nitrogen (98.7 vol.%) is added as the carbon precursor for the growth of CNTs on CFs (30 min). The resultant fibers were collected on a motorized spool which determined the pull-though rate during the reaction (1.2 m/h), and were used as synthesized (hereafter referred to as CNT-g-CFs). As a control sample, pre-deposited bi-catalyst precursors coated CF samples which have passed through the continuous and open reactor at 770 °C, in an inert carrier gas with hydrogen reduction at 1.2 m h/h (as previously described), but without the carbon feedstock, are hereafter referred to as heated and reduced bi-catalyst coated carbon fibers (HRBC-CFs).

2.3 Fiber surface characterization

The surface topography of CFs was characterized by SEM (Carl Zeiss MERLIN Compact, DE) using an acceleration voltage of 20 kV and working distance ranging from 7 mm to 15 mm. Additional high resolution micrographs were taken by a field emission SEM (Carl Zeiss Leo Gemini 1525, GB) operated at 5 kV, and working distance ~10 mm, with the samples prepared on aluminum substrate and adhered with silver dag (not sputtered). Fracture surfaces of composite specimens were sputter-coated (Gatan 682 Precision Etching and Coating System, US) with gold prior to imaging. Moreover, a scanning transmission electron microscope (TEM, FEI Tecnai G2 F30, NL) was applied to characterize the morphology of CNTs growth on the CF surface.

The surface topography of the CFs was further examined by atomic force microscopy (AFM)

(Dimension icon, Veeco, US) using an antimony-doped silicon probe (FMV-A, Bruker, US) and operated in tapping mode. The scan areas were 4 × 4 µm and 1 × 1 µm for low and high magnification topographical images, respectively. Images were analyzed using the software (NanoScope Analysis) to obtain the arithmetic average roughness (R_a) calculated from four positions with the areas of 200 × 200 nm, and the surface area ratio (r). The parameter r is defined as the ratio between the area (A) of the topography determined by AFM, and the geometrically projected area (A_g) of the topography:

$$r = \frac{A}{A_g} \quad (1).$$

the elemental surface composition and oxidation state of the elements present was determined by measuring XPS wide scan spectra in the energy range from 0 to 1350 eV using a Thermo Fisher Scientific (ESCALAB 250xi, US). Short sections, two cm in length, were cut carefully from the fiber tows (12k) and clamped securely in a steel sample holder. The XPS interaction spot size is approx. 900 µm (diameter), which corresponds to an irradiated area containing roughly 120 fibers for each sample set. The high resolution C(1s) and O(1s) XPS spectra were obtained to determine the concentrations of carbon- or oxygen-containing functional groups on the surface of CF samples.

2.4 Fiber surface contact angle measurements via Wilhelmy method

The gravimetric Wilhelmy method uses test liquids with known surface energy (components) but different polar and dispersive contributions to obtain information about the surface chemistry of the fibers. The Wilhelmy method used here has been described in detail elsewhere [32,33,36], but in brief, the advancing and receding contact angles are determined using a high-precision tensiometer (resolution 1 µg, K100SF Krüss, GE) and three test liquids, deionized water (DW, resistivity 18.2 MΩ cm at 25 °C), ethylene glycol (EG, Sigma–Aldrich, assay 99 %), and diiodomethane (DIM, Merck, assay 99 %). At least three fibers were sampled for each test liquid, which were immersed into and withdrawn from the test

liquid three times, repeatedly, at a velocity of 3 mm/min to measure the wetting forces exerted on the fibers. The measured forces and the diameter of each fiber (measured by SEM after wetting test) were used to calculate the advancing (θ_a) and receding contact angles (θ_r) and the contact angle hysteresis ($\Delta\theta$) with $\Delta\theta = \theta_a - \theta_r$. The equilibrium contact angle (θ_{equ}) is then obtained by [44];

$$cos\ \theta_{equ} = 0.5\ cos\ \theta_a + 0.5\ cos\ \theta_r \quad (2).$$

2.5 Surface energy components and work of adhesion calculations

The van Oss acid-base theory [45] allows for the determination of the Lifshitz-van der Waals γ^{LW} and acid-base γ^{AB}, surface energy components as well as the Lewis acid γ^+ and base γ^- surface energy parameters of the solid surface free tension [35] based on the equilibrium contact angle θ according to Equation 3 (in its matrix notation),

$$\boldsymbol{Ax} = \boldsymbol{b} \quad (3)\ ,$$

where,

$$\boldsymbol{A} = \begin{bmatrix} \sqrt{\gamma_{l,1}^{LW}} & \sqrt{\gamma_{l,1}^{+}} & \sqrt{\gamma_{l,1}^{-}} \\ \sqrt{\gamma_{l,2}^{LW}} & \sqrt{\gamma_{l,2}^{+}} & \sqrt{\gamma_{l,2}^{-}} \\ \cdots & \cdots & \cdots \\ \sqrt{\gamma_{l,m}^{LW}} & \sqrt{\gamma_{l,m}^{+}} & \sqrt{\gamma_{l,m}^{-}} \end{bmatrix}, \boldsymbol{x} = \begin{bmatrix} \sqrt{\gamma_s^{LW}} \\ \sqrt{\gamma_s^{-}} \\ \sqrt{\gamma_s^{+}} \end{bmatrix}, \boldsymbol{b} = \begin{bmatrix} 0.5\gamma_{l,1}(1+cos\theta_1) \\ 0.5\gamma_{l,2}(1+cos\theta_2) \\ \cdots \\ 0.5\gamma_{l,m}(1+cos\theta_m) \end{bmatrix},$$

with the symbols "*l*" and "*s*" referring liquid and solid, respectively, and the numerical digit in the subscript of symbol denoting various test liquids. No less than three test liquids can be used to solve Equation 3 readily. In order to lower the sensitivity of the calculation to variations of contact angle values, a liquid triplet with the lowest possible condition number needs to be selected. A low condition number normally corresponds to a well-balanced set of test liquids, in which dispersive and non-dispersive liquids are chosen in particular, hence the use of DIM, DW and EG in this study [46,47]. The condition number is defined as:

$$cond\ (\boldsymbol{A}) = \|\boldsymbol{A}\|\|\boldsymbol{A}^{-1}\| \quad (4),$$

where $\boldsymbol{A}$ is the matrix in Equation 3, $\|\ \|$ denotes the matrix norm $\|\boldsymbol{A}\|$. The calculation of surface energy components was performed by using SurfTen v4.3 software as depicted in previous work [48]. The thermodynamic work of adhesion $W_a = \gamma_s + \gamma_l - \gamma_{sl}$ was then determined from the calculated surface energy. It is used to predict the bonding between reinforcements and polymer matrices in composites [30,49–51].

2.6 Single fiber microdroplet debond test

Microdroplet debond tests were performed to measure the apparent interfacial shear strength τ_{IFSS} between fibers and polymer matrices using an interface strength tester (East Wing Industrial, MODEL HM410, JP). Samples for the single fiber microdroplet debond tests were prepared by gluing single fibers taken from the tow onto a steel frame. Pellets of PP were melted on a clean glass slide by heating on a heating stage to 235 °C for 5 min. Then, suspended single fibers specimens were dipped into the molten PP and withdrawn to form PP microdroplets around the CF. Finally, the composite specimens were placed into a vacuum oven at 235 °C for 5 min to melt the polymer matrices once again, to achieve completely shaped single fiber microdroplet specimens. Each tested microdroplet was gripped between two movable metal blades and the CF pulled out of the microdroplet at a steady speed of 0.1 mm/min, while measuring the force-displacement via a computer interface, shown in Figure 1. An optical microscope was applied to measure the embedded length (l_e), whilst positioning the blade edges and monitoring the testing process. The embedded fiber areas (A_e) can be calculated according to Equation 5;

$$A_e = \pi d_f l_e \quad (5),$$

where CF diameter (d_f) was measured by SEM for each sample after fracture. The average τ_{IFSS} was determined by the linear fit to the plot of peak debonding force (F_{max}) over A_e, $F_{max} = f(A_e)$ fixed

through the origin with tests resulting in fractured droplets omitted. At least 33 specimens for each material were used for a robust evaluation.

3. Results and discussion

3.1 Surface morphology and roughness of the fiber surfaces

The surface morphology of fibers was studied using SEM and representative images are shown in Figure 2. The as-received unsized and sized fibers have the typical grooves (crenulations) on their surfaces. They are very similar in their appearance, with no discernable differences resulting from the application of the sizing by the manufacturer.

The HRBC-CFs showed catalyst particles with diameters in the order of 10 nm after exposing the precursors to a reducing gas environment at high temperature. The surfaces of the CNT-g-CFs were covered with a rough and porous layer made of short CNTs with an average height varying around an average value of 140 nm (perpendicular length from the fiber surface shown in Figure S1, observed in SEM and TEM) in agreement with previous results [20], with diameters on the order of 10 nm observed in TEM. Both, the HRBC-CF and CNT-g-CF appeared undamaged, as also found previously [20].

AFM topographical images confirmed the SEM observations (Figure 3). The sizing applied to carbon fibers is well known to smooth the surface, and protects the fibers during handling when compared to their unsized counterpart. On the other hand, CNT coated carbon fibers had the highest surface roughness; $R_a$determined by AFM increased from sized CFs (0.83 ± 0.07 nm) < unsized CFs (1.35 ± 0.31 nm) ≈ HRBC-CFs (1.37 ± 0.24 nm) < CNT-g-CFs (3.71 ± 0.43 nm). It should be noted that the roughness of the CNT-g-CFs, observed in the SEM images, may be underestimated by the AFM measurements as the cantilever tip radius (8 nm) is almost as large as the CNT diameter.

3.2 Wetting behavior of the fiber surfaces

Typical dynamic contact angle cycles (advancing and receding) of diiodomethane on fibers are shown in Figure 4. During the first wetting cycle, an unsteady pre-force was occasionally discovered [32], resulting in unreasonable contact angle results. During this first cycle, the porous CNT layer also imbibes the liquids. The force induced by the wicking process is, however, negligible compared to the force emerging from the formation of menisci around the fibers [36]. Due to these unsteady forces, dynamic contact angles were calculated only during the last two cycles. The contact angle versus position curves along the fibers were in good agreement with surface irregularities, indicating that contact angle fluctuations are related to topographical features of the CF surfaces. For HRBC-CFs and CNT-g-CFs, the pinning and jumping of the contact line in the wetting cycles are due to the topography of the fiber surface, which affects the local contact angle values [36]. Compared to sized CFs and HRBC-CFs, CNT-g-CFs have more scattered contact angle values caused by higher surface roughness variations (Figure 4 d). The wetting cycles for DW and EG showed identical trends related to surface roughness and can be found in the Supplementary material, Figure S2 and Figure S3. In one instance, the local surface microstructure (SEM) for CNT-g-CF was directly associated with one of the fluctuations seen in the wetting cycles (Figure S2 g) and h)). For the sized CFs and HRBC-CFs, contact angles fluctuated to a smaller extent due to their relatively smooth and homogeneous surfaces.

The average advancing and receding contact angles of DW, EG and DIM are provided in Table 1, as well as the θ_{equ} and $\Delta\theta$, which were calculated based on the method mentioned in Section 2.4. All CFs were hydrophobic with advancing contact angles, measured during wetting of dry surfaces, characteristic for the lower surface energy part of the fiber surfaces, $\vartheta_a > 70^\circ$, however, catalyst deposition and thermal treatment rendered the fibers more hydrophobic due to the expected loss of the oxygen-containing

functional groups on the industrially oxidized fibers. Comparing with HRBC-CFs, the θ_r and corresponding θ_{equ} from CNT-g-CFs in all test liquids decreased due to the pinning of the contact line. All the fibers show obvious contact angle hysteresis but $\Delta\theta$ from CNT-g-CFs is the highest when compared to the baseline samples. Increased pinning might be due to the nanotubes induced rougher surface and the surface chemical heterogeneity.

The Wenzel model is widely used to link the apparent contact angle of a liquid on a rough surface with the intrinsic contact angle. Meanwhile, the porous CNT layer on the surface of CNT-g-CFs can be recognized as a rough surface formed by the presence of CNTs, which can yield lower contact angles compared to the contact angles on a smooth surface [36]. Consequently, the equilibrium contact angles on "roughness corrected CNT-g-CFs" hereafter denoted with *, ($\theta_{equ\ (CNT-g-CF*)}$), can be calculated theoretically based on equilibrium contact angles of CNT-g-CF ($\theta_{equ\ (\mathrm{CNT-g-CF})}$) according to the Wenzel model, expressed as Equation 6;

$$cos\,\theta_{equ\ (CNT-g-CF)} = r\,cos\,\theta_{equ\ (CNT-g-CF*)} \quad (6)$$

Using the approach mentioned in Section 2.3, the value of r can be estimated according to the AFM images, for CNT-g-CF a value of r 1.176 ± 0.007 was determined using Figure 3 k). Consequently, the equilibrium contact angle for CNT-g-CFs* in DW was derived to be 79.6 ± 3.1° (Table 1), which is comparable with Zhang *et al*. [36](~ 84°) using the same approach, and the calculated value by Neimark *et al*. [52] (~ 82°). The estimated contact angle values of CNTs in EG and DIM were also in agreement with those estimated by Zhang *et al*. [36], which further validates the use of the Wenzel model for CNT-g-CF samples, and represents an appropriate approximation.

3.3 Surface energy components and thermodynamic work of adhesion

Surface energy components (Table 2) were determined using the equilibrium contact angles obtained in Section 3.2 using the Della Volpe-Siboni scale [48]. The selected liquid triplet presents condition numbers from 3.57 to 4.25. These values are lower than the other triplets reported in literature [46,47], representing to a better set of test liquids. The total surface energy was highest for CNT-g-CFs, with the other CF samples within error of each other. The total surface energy contribution calculated from $\theta_{equ\ (CNT-g-CF*)}$ is 35.6 mJ/m^2 (theoretically estimated equilibrium contact angles on CNT-g-CFs*), which is comparable to literature values for multi-walled CNTs (ca. 37 mJ/m^2) [36]. The sized CF and unsized CFs had indistinguishable surface energy components. The polar contributions on the HRBC-CFs, and CNT-g-CFs* surfaces are lower than for the unsized/sized CFs, as surface oxides decompose at elevated temperatures [53,54], for instance those experienced during the reductive gas exposure or during CNT-growth. Existing research recognizes that γ^{LW} demonstrates the surface characteristics of untreated CFs [53], as surfaces are mostly composed of graphitized aromatic rings. Grafting CNTs on CFs further increases the aromatic carbon contribution as evidenced by the high γ^{LW} and low γ^{AB} obtained for the CNT-g-CFs*.

The calculated wetting parameters for the CFs with hydrophobic PP are shown in Table 2. HRBC-CFs, sized CFs and unsized CFs are likely to have a very similar adhesion with PP owing to their similar work of adhesion, ca. 63 and 64 mJ/m^2. CNT-g-CFs showed the highest work of adhesion, ca. 71 mJ/m^2, which is indicative of the higher potential adhesion with PP, based simply on chemistry. However, since the CNT-g-CFs surfaces are also rough, the wetting parameters for CNT-g-CF* (roughness corrected) were also determined based on the surface energies of CNT-g-CFs* and PP.

3.4 Surface composition of the fiber surfaces

The XPS spectra of the four CF samples demonstrated visible carbon and oxygen peaks (presented in the Supplementary material, Figure S4), representing the major near-surface constituents of the CFs investigated; as expected for a commercially supplied CF. Near-surface element compositions were determined via quantitative peak analysis (Table 3). Bulk carbon contents for both AS4 (unsized CF) and AS4C (sized CF) are listed as 94% on the manufacturer's datasheets, as determined by elemental analysis. The XPS determined carbon composition for as-received unsized CF and sized CF samples are somewhat lower, as the technique is more sensitive to the modified surface chemistry; indeed, the carbon, oxygen, nitrogen, and silicon XPS compositions are close to literature values [55–57]. The increased silicon content for unsized CFs is attributed to contamination; the composition of epoxy compatible sizing on sized CFs is proprietary information. HRBC-CFs samples showed small amounts of iron and nickel which remained on the surface after catalyst precursor deposition and processing, in addition to any residual decomposed sizing. The (partial) reduction or atmospheric re-oxidation of the catalyst particles in HRBC-CF samples will increase the surface oxygen content. The near-surface atomic composition of CNT-g-CFs, are strongly influenced by the grafted CNTs, which dominate the interaction volume analyzed by XPS. Since this layer is less dense (porous), the total interaction volume is likely to be increased. The carbon and oxygen concentrations for CNT-g-CF are consistent with those previously reported for carbon nanotubes [58]. The increased iron content for CNT-g-CF is associated with the remaining catalyst particles; exposed metal may also oxidise but typically catalyst particles remain metallic after growth as they are encapsulated within the CNTs. The lack of a nickel signal in CNT-g-CF, was unexpected, but may indicate that the tip growth catalyst is predominantly iron while the nickel plays a role in conditioning the catalyst during initial reduction or nucleation. Literature reports a shielding effect of the CNT walls when the nickel particles are

loaded within the internal channels, which significantly attenuates the nickel signal [59]. The detailed mechanism for the CNT growth promotion observed on applying a potential difference to the CF substrate is not yet known.

The increased γ^{LW} component observed for CNT-g-CFs* by the wetting experiments, is consistent with the XPS data showing a high surface carbon content. The changes in surface energy (γ^{LW}) correlate well with the C/O ratios determined by XPS analysis (Figure 5).

3.5 Microdroplet interfacial shear strength

Microdroplet single fiber reinforced PP composites were tested with tabulated averages detailed in Table 4; the linear fit for deboning force against embedded area are given in the Supplementary Information (Figure S5). The IFSS of the CNT-g-CF/PP system increased by 39%, 40% and 53% compared to sized CFs, HRBC-CFs and unsized CFs, respectively. The IFSS of CNT-g-CF/PP composites (11.2 ± 0.3 MPa) measured here is in the order of results demonstrated in the previous work for other nanostructured CF surface modified/PP composites (10.7 MPa for plasma treated and zinc oxide nanorod modified CF/PP composites) [11]. Yumitori *et al*. reported that growing CNTs (~350 nm in length and 20-60 nm in diameter) on carbon fibers improved the IFSS with PP by 35% compared to desized (in acetone) CFs [19]. The larger improvement (53% compared to unsized fibers) observed in the current study can be attributed to the smaller CNT diameter (~10nm) which is associated with higher roughness and potentially high CNT crystalline quality, although the choice of PP grade may contribute [60]. In addition, in contrast to Yumitori's batch processing, the continuous grafting process provides a more consistent and practical CNT-g-CF material.

Fractography showed that the PP droplets were fully debonded upon failure for all samples and that the fracture surfaces are smooth without residual PP matrix (Figure 6 a) - c)). This failure mode implies

adhesive failure at the fiber-matrix interface/interphase. The similar failure surfaces of the unsized CF, sized CF, and HRBC-CFs IFSS samples are consistent with the numerical data showing that sizing, catalyst precursor deposition and thermal treatment processes had little effect on mechanical interfacial/interphase performance in PP. In contrast, CNT-g-CF (Figure 6 d), e)) showed a rougher fracture CF surface, consistent with an intermediate cohesive failure closer to the ends of the CNTs-matrix region. A rougher fractured CNT-g-CF surface, with remnants of PP matrix indicates good interfacial adhesion between the nanotubes and the polymer matrices, with the failure stress concentration altered from CF-matrix interphase, as predicted in models for a uniform and short array of CNTs on the CF surface [61].

The predicted work of adhesion is unable to show a distinct trend for the improved IFSS. The predicted work of adhesion for CNT-g-CF* increased by 4% compared to unsized CFs, which is smaller than that for CNT-g-CFs (11%). However, the increase of the IFSS is up to 53%, indicating that mechanical keying, rather than thermodynamic adhesion, is the dominant mechanism for the IFSS improvement. The predicted work of adhesion addresses adhesion dominated by adsorption mechanisms while it fails to account for mechanical key, strain energy dissipation (plastic deformation of the matrix), and the residual radial compressive stresses at the interface [62], thereby underestimating the observe IFSS increase. Nevertheless, the IFSS results are in agreement with the measured contact angles for CFs in DIM (Figure 6 f)). As an exclusively dispersive liquid, DIM could be considered to a model for PP in order to predict the extent of wetting by the polymer, an essential prerequisite to establish intimate contacts between the CF surface and PP, crucial for mechanical interlocking.

4. Conclusions

Grafting CNTs on CF is an effective approach to improving the interfacial interactions in composite materials. The continuous process illustrated here provides larger quantities of consistent CNT-g-CF that

may be scaled up to full composite testing in the near future. Significantly, the process has been optimized to create short, small diameter CNTs, that are most appropriate for interfacial reinforcement in fiber composites. The small diameter maximizes the surface area available for wetting interactions, whilst the short length will not impede primary CF packing; in addition, shorter CNTs have already been shown to be more effective for improving IFSS in glass fiber – epoxy systems due to an improvement morphology and cohesive fracture mode [63]. Importantly, the continuous approach is compatible with existing carbon fiber production equipment and may be ultimately implemented commercially.

CNT-g-CFs are particularly attractive in unreactive thermoplastic matrices where wetting and adhesion typically limit composite performance, especially when using polyolefin matrices, such as PP. Wetting measurements establish the intrinsic chemistry of the grafted material, which is dominated by non-polar, van der Waals interactions. These non-polar interactions allow full wetting of the convoluted CNT network by the non-polar PP matrix, a crucial pre-requisite for interfacial adhesion. Indeed, extensive microdroplet testing proves that the grafting of the CNTs significantly improves the IFSS compared to the appropriate control samples (up to +53%). However, the predicted work of adhesion deduced from the wetting measurements underestimates the observe IFSS increase, as it does not account for the mechanical keying between the polymer and the CNT network. This interaction is evidenced in the fractography which shows a change in failure mode to a cohesive fracture of the CNT-reinforced interphase, rather than a simple interfacial de-adhesion. Guided by wetting measurements, the CNT-g-CF system can be adapted to a wide range of matrices. The expected thermal stability of the CNT-g-CF and the mechanical keying interactions implies that the approach may be useful for high performance matrices processed at elevated temperatures where conventional CF surface chemistry is degraded [64]. CNT-g-CF are, therefore, a promising generic technology for enabling future thermoplastic-matrix carbon fiber composites.

Acknowledgements

The authors would like to thank the supported from the Interuniversity Attraction Poles Programme (IAP 7/38 MicroMAST) initiated by the Belgian Science Policy Office. J.W. was also supported by the Natural Science Foundation of Shandong Province, China (ZR2020QE080) and China Scholarship Council Scholarships during his placement at KU Leuven. The authors D.B.A., H.G.D.L., A.B., and M.S.P.S. would like to thank the UK Engineering and Physical Sciences Research Council (EPSRC) (EP/P502500/1), EPSRC Impact Acceleration: Pathways to Impact Award (EP/K503733/1) and Weizmann UK Programme Grant, The Weizmann Institute of Science, Hierarchical composites based on carbon nanotube fibres (2012-2015) for financial support of this work. In addition, H.G.D.L. would like to thank Lloyd's Register Foundation for financial support. We thank Hexcel for supplying the AS4C and AS4 carbon fibers.

References

[1] Offringa AR. Thermoplastic composites - Rapid processing applications. Compos Part A Appl Sci Manuf 1996;27:329–36.

[2] Wong KH, Syed Mohammed D, Pickering SJ, Brooks R. Effect of coupling agents on reinforcing potential of recycled carbon fibre for polypropylene composite. Compos Sci Technol 2012;72:835–44.

[3] Mäder E, Grundke K, Jacobasch HJ, Wachinger G. Surface, interphase and composite property relations in fibre-reinforced polymers. Composites 1994;25:739–44.

[4] Karger-Kocsis J, Mahmood H, Pegoretti A. Recent advances in fiber/matrix interphase engineering for polymer composites. Prog Mater Sci 2015;73:1–43.

[5] Schaefer JD, Rodriguez AJ, Guzman ME, Lim CS, Minaie B. Effects of electrophoretically deposited carbon nanofibers on the interface of single carbon fibers embedded in epoxy matrix. Carbon 2011;49:2750–9.

[6] Drzal LT, Sugiura N, Hook D. The role of chemical bonding and surface topography in adhesion between carbon fibers and epoxy matrices. Compos Interfaces 1996;4:337–54.

[7] Fuentes CA, Tran LQN, Van Hellemont M, Janssens V, Dupont-Gillain C, Van Vuure AW, et al. Effect of physical adhesion on mechanical behaviour of bamboo fibre reinforced thermoplastic composites. Colloids Surfaces A Physicochem Eng Asp 2013;418:7–15.

[8] Han SH, Oh HJ, Kim SS. Evaluation of fiber surface treatment on the interfacial behavior of carbon fiber-reinforced polypropylene composites. Compos Part B Eng 2014;60:98–105.

[9] Gassan J, Bledzki AK. The influence of fiber-surface treatment on the mechanical properties of jute-polypropylene composites. Compos Part A Appl Sci Manuf 1997;28:1001–5.

[10] Tang J, Swolfs Y, Aslani A, Mencattelli L, Bullegas G, Pinho ST, et al. Engineering tensile behavior of hybrid carbon fiber/self-reinforced polypropylene composites by bio-inspired fiber discontinuities. Compos Part B Eng 2019;178:107502.

[11] Song SA, Lee CK, Bang YH, Kim SS. A novel coating method using zinc oxide nanorods to improve the interfacial shear strength between carbon fiber and a thermoplastic matrix. Compos Sci Technol 2016;134:106–14.

[12] Zhang S, Liu WB, Hao LF, Jiao WC, Yang F, Wang RG. Preparation of carbon nanotube/carbon fiber hybrid fiber by combining electrophoretic deposition and sizing process for enhancing interfacial strength in carbon fiber composites. Compos Sci Technol 2013;88:120–5.

[13] Liu Y, Zhang X, Song C, Zhang Y, Fang Y, Yang B, et al. An effective surface modification of carbon fiber for improving the interfacial adhesion of polypropylene composites. Mater Des 2015;88:810–9.

[14] Zhang G, Sun S, Yang D, Dodelet JP, Sacher E. The surface analytical characterization of carbon fibers functionalized by H2SO4/HNO3 treatment. Carbon 2008;46:196–205.

[15] Shazed MA, Suraya AR, Rahmanian S, Mohd Salleh MA. Effect of fibre coating and geometry on the tensile properties of hybrid carbon nanotube coated carbon fibre reinforced composite. Mater Des 2014;54:660–9.

[16] Qian H, Bismarck A, Greenhalgh ES, Shaffer MSP. Carbon nanotube grafted carbon fibres: A study of wetting and fibre fragmentation. Compos Part A Appl Sci Manuf 2010;41:1107–14.

[17] Wang C, Li Y, Tong L, Song Q, Li K, Li J, et al. The role of grafting force and surface wettability in interfacial enhancement of carbon nanotube/carbon fiber hierarchical composites. Carbon 2014;69:239–46.

[18] He X, Zhang F, Wang R, Liu W. Preparation of a carbon nanotube/carbon fiber multi-scale reinforcement by grafting multi-walled carbon nanotubes onto the fibers. Carbon 2007;45:2559–63.

[19] Yumitori S, Arao Y, Tanaka T, Naito K, Tanaka K, Katayama T. Increasing the interfacial strength in carbon fiber/polypropylene composites by growing CNTs on the fibers. WIT Trans Modelling Simul 2013;55:275–84.

[20] Anthony DB, Sui XM, Kellersztein I, De Luca HG, White ER, Wagner HD, et al. Continuous carbon nanotube synthesis on charged carbon fibers. Compos Part A Appl Sci Manuf 2018;112:525–38.

[21] Zheng L, Wang Y, Qin J, Wang X, Lu R, Qu C, et al. Scalable manufacturing of carbon nanotubes on continuous carbon fibers surface from chemical vapor deposition. Vacuum 2018;152:84–90.

[22] Lyu H, Jiang N, Li Y, Lee H, Zhang D. Enhanced interfacial and mechanical properties of carbon fiber / PEEK composites by hydroxylated PEEK and carbon nanotubes. Compos Part A 2021;145:106364.

[23] Li Q, Church JS, Naebe M, Fox BL. Interfacial characterization and reinforcing mechanism of novel carbon nanotube – Carbon fibre hybrid composites. Carbon 2016;109:74–86.

[24] Stojcevski F, Randall JD, Henderson LC. Using variable interfacial adhesion characteristics within a composite to improve flexural strength and decrease fiber volume. Compos Sci Technol 2018;165:250–8.

[25] Zhang X, Fan X, Yan C, Li H, Zhu Y, Li X, et al. Interfacial microstructure and properties of carbon fiber composites modified with graphene oxide. ACS Appl Mater Interfaces 2012;4:1543–52.

[26] Jones AR, Cintora A, White SR, Sottos NR. Autonomic healing of carbon fiber/epoxy interfaces. ACS Appl Mater Interfaces 2014;6:6033–9.

[27] Qian H, Bismarck A, Greenhalgh ES, Kalinka G, Shaffer MSP. Hierarchical composites reinforced with carbon nanotube grafted fibers: The potential assessed at the single fiber level. Chem Mater 2008;20:1862–9.

[28] Zhang L, De Greef N, Kalinka G, Van Bilzen B, Locquet JP, Verpoest I, et al. Carbon nanotube-grafted carbon fiber polymer composites: Damage characterization on the micro-scale. Compos Part B Eng 2017;126:202–10.

[29] Agnihotri P, Basu S, Kar KK. Effect of carbon nanotube length and density on the properties of carbon nanotube-coated carbon fiber/polyester composites. Carbon 2011;49:3098–106.

[30] Connor M, Bidaux JE, Månson JAE. A criterion for optimum adhesion applied to fibre reinforced composites. J Mater Sci 1997;32:5059–67.

[31] Lee YIN, Chiao SM. Visualization of dynamic contact angles on cylinder and fiber. J Colloid Interface Sci 1996;181:378–84.

[32] Qiu S, Fuentes CA, Zhang D, Van Vuure AW, Seveno D. Wettability of a single carbon fiber. Langmuir 2016;32:9697–705.

[33] Wang J, Fuentes CA, Zhang D, Wang X, Van Vuure AW, Seveno D. Wettability of carbon fibres at micro- and mesoscales. Carbon 2017;120:438–46.

[34] Bismarck A, Kumru ME, Song B, Springer J, Moos E, Karger-Kocsis J. Study on surface and mechanical fiber characteristics and their effect on the adhesion properties to a polycarbonate matrix tuned by anodic carbon fiber oxidation. Compos Part A Appl Sci Manuf 1999;30:1351–66.

[35] van Oss CJ, Chaudhury MK, Good RJ. Monopolar surfaces. Adv Colloid Interface Sci 1987;28:35–64.

[36] Zhang L, Wang J, Fuentes CA, Zhang D, Van Vuure AW, Seo JW, et al. Wettability of carbon nanotube fibers. Carbon 2017;122:128–40.

[37] Bismarck A, Richter D, Wuertz C, Springer J. Basic and acidic surface oxides on carbon fiber and their influence on the expected adhesion to polyamide. Colloids Surfaces A Physicochem Eng Asp 1999;159:341–50.

[38] Lu C, Wang J, Lu X, Zheng T, Liu Y, Wang X, et al. Wettability and Interfacial Properties of Carbon Fiber and Poly(ether ether ketone) Fiber Hybrid Composite. ACS Appl Mater Interfaces 2019;11:31520–31.

[39] Pisanova E, Zhandarov S, Mäder E. How can adhesion be determined from micromechanical tests? Compos Part A Appl Sci Manuf 2001;32:425–34.

[40] Dilsiz N, Wightman JP. Effect of acid-base properties of unsized and sized carbon fibers on fiber/epoxy matrix adhesion. Colloids Surfaces A Physicochem Eng Asp 2000;164:325–36.

[41] Tran MQ, Ho KKC, Kalinka G, Shaffer MSP, Bismarck A. Carbon fibre reinforced poly(vinylidene fluoride): Impact of matrix modification on fibre/polymer adhesion. Compos Sci Technol 2008;68:1766–76.

[42] Ho KKC, Lamoriniere S, Kalinka G, Schulz E, Bismarck A. Interfacial behavior between atmospheric-plasma-fluorinated carbon fibers and poly(vinylidene fluoride). J Colloid Interface Sci 2007;313:476–84.

[43] Volpe C Della, Siboni S. Acid-base surface free energies of solids and the definition of scales in the Good-van Oss-Chaudhury theory. J Adhes Sci Technol 2000;14:235–72.

[44] Andrieu C, Sykes C, Brochard F. Average Spreading Parameter on Heterogeneous Surfaces. Langmuir 1994;10:2077–80.

[45] van Oss CJ, Good RJ, Chaudhury MK. Additive and nonadditive surface tension components and

the interpretation of contact angles. Langmuir 1988;4:884–91.
[46] Della Volpe C, Siboni S. Some reflections on acid-base solid surface free energy theories. J Colloid Interface Sci 1997;195:121–36.
[47] Della Volpe C, Maniglio D, Brugnara M, Siboni S, Morra M. The solid surface free energy calculation: I. In defense of the multicomponent approach. J Colloid Interface Sci 2004;271:434–53.
[48] Della Volpe C, Maniglio D, Siboni S, Morra M. Recent theoretical and experimental advancements in the application of van Oss-Chaudury-Good acid-base theory to the analysis of polymer surfaces I. General aspects. J Adhes Sci Technol 2003;17:1477–505.
[49] Packham DE. Work of adhesion: Contact angles and contact mechanics. Int J Adhes Adhes 1996;16:121–8. https://doi.org/10.1016/0143-7496(95)00034-8.
[50] Wu S. Polar and nonpolar interactions in adhesion. J Adhes 1973;5:39–55.
[51] Wu S. Polymer Interface and Adhesion. New York: Basel: Marcel Dekker; 1982.
[52] Neimark A V. Thermodynamic equilibrium and stability of liquid films and droplets on fibers. J Adhes Sci Technol 1999;13:1137–54.
[53] Bismarck A, Wuertz C, Springer J. Basic surface oxides on carbon fibers. Carbon 1999;37:1019–27.
[54] Ramanathan T, Bismarck A, Schulz E, Subramanian K. Investigation of the influence of acidic and basic surface groups on carbon fibres on the interfacial shear strength in an epoxy matrix by means by single-fibre pull-out test. Compos Sci Technol 2001;61:599–605.
[55] Xie Y, Sherwood PMA. AS4 PAN-based Carbon Fiber by Core Level and Valence Band XPS. Surf Sci Spectra 1992;1:306–11.
[56] Nairn JA, Harper SI, Bascom WD. Effects Carbon of Fiber, Matrix, Fiber Composite and Interphase Compression on Strength. NTRS - NASA Tech Reports 1994.
[57] Lee WH, Lee JG, Reucroft PJ. XPS study of carbon fiber surfaces treated by thermal oxidation in a gas mixture of O2/(O2+N2). Appl Surf Sci 2001;171:136–42.
[58] Okpalugo TIT, Papakonstantinou P, Murphy H, McLaughlin J, Brown NMD. High resolution XPS characterization of chemical functionalised MWCNTs and SWCNTs. Carbon 2005;43:153–61.
[59] Ma Q, Wang D, Wu M, Zhao T, Yoneyama Y, Tsubaki N. Effect of catalytic site position: Nickel nanocatalyst selectively loaded inside or outside carbon nanotubes for methane dry reforming. Fuel 2013;108:430–8.
[60] Yamaguchi A, Hashimoto T, Uematsu H, Urushisaki M, Sakaguchi T, Takamura A, et al. Investigation of interfacial adhesion of telechelic polypropylenes for carbon fiber-reinforced plastics. Polym J 2020;52:413–9.
[61] Liu Q, Lomov S V., Gorbatikh L. When does nanotube grafting on fibers benefit the strength and toughness of composites? Compos Sci Technol 2020;188:107989.
[62] Thomason JL, Yang L. Temperature dependence of the interfacial shear strength in glass-fibre polypropylene composites. Compos Sci Technol 2011;71:1600–5.
[63] De Luca HG, Anthony DB, Greenhalgh ES, Bismarck A, Shaffer MSP. Piezoresistive structural composites reinforced by carbon nanotube-grafted quartz fibres. Compos Sci Technol 2020;198:108275.
[64] Karsli NG, Ozkan C, Aytac A, Deniz V. Effects of sizing materials on the properties of carbon fiber-reinforced polyamide 6,6 composites. Polym Compos 2013;34:1583–90.

Figures and tables

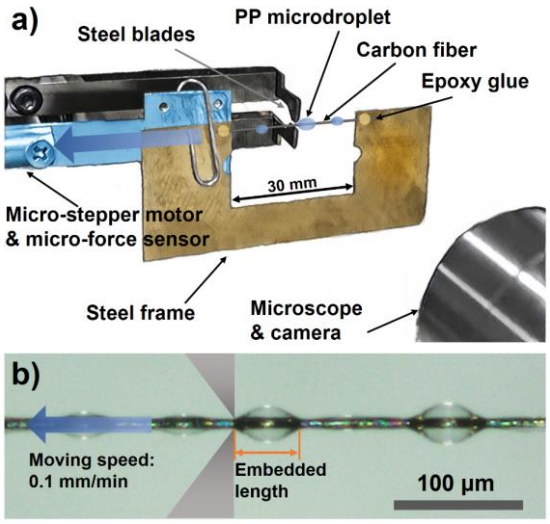


Figure 1: Schematic diagram of the microdroplet test; a) test apparatus (the tested fiber and the PP microdroplets are not to scale), and b) optical image of the single fiber composite specimen. [Color image]

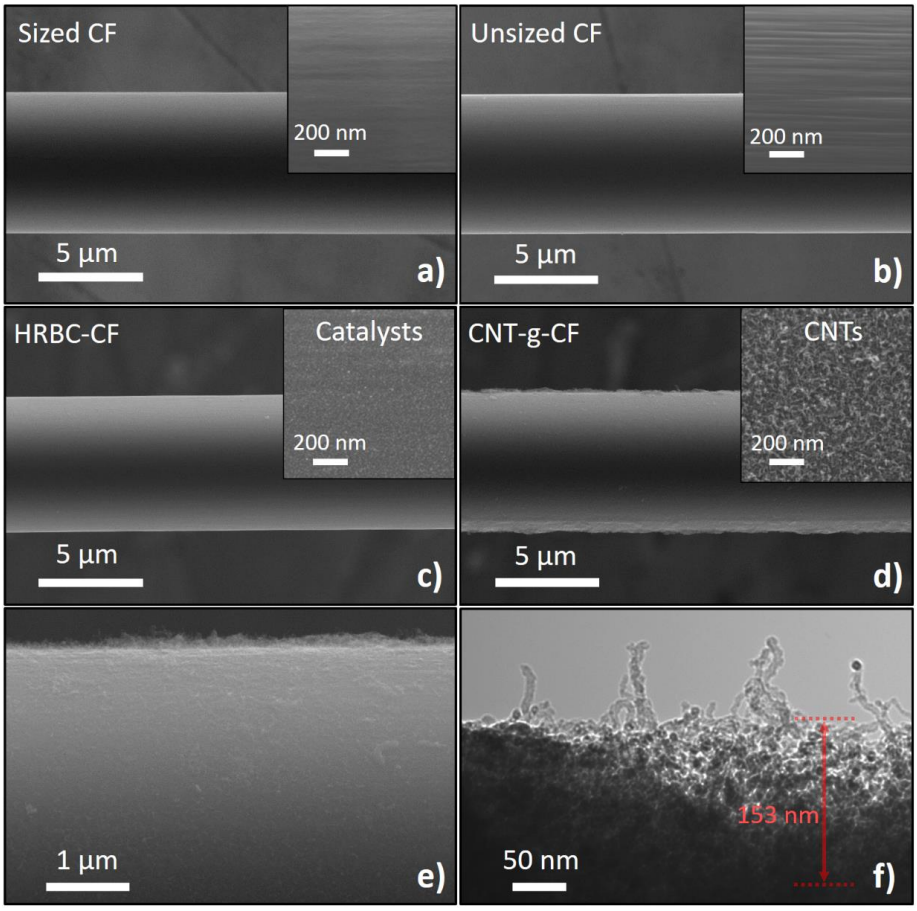


Figure 2: Scanning electron micrographs of carbon fibers: a) as-received sized CF, b) unsized CF, c) HRBC-CF, d) CNT-g-CF, with high resolution inserts of the fiber surfaces. e) SEM micrograph of CNT layer on the surface of CNT-g-CFs and f) TEM micrograph of CNT-g-CFs surface. [Color image]

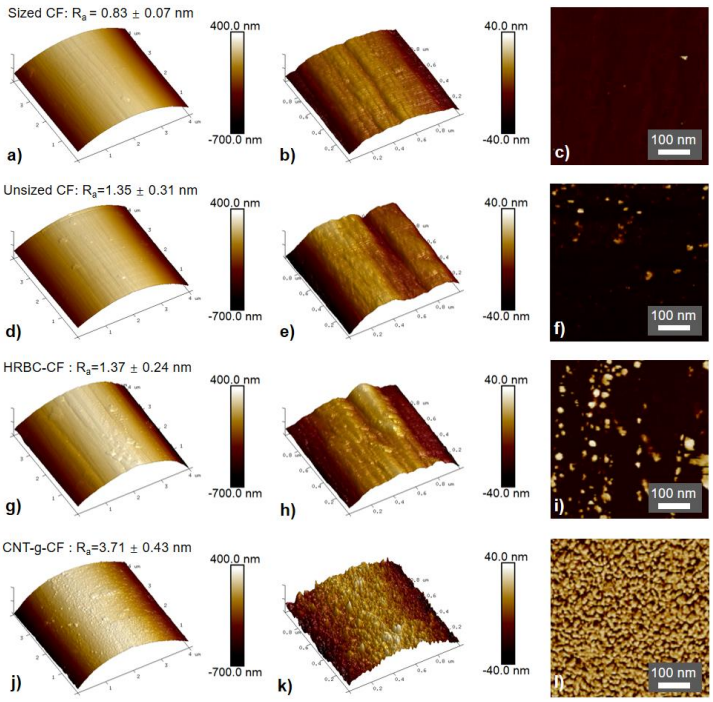


Figure 3: AFM topographical images and surface roughness (R_a) of carbon fibers: sized CF at low magnification (4x4 µm²) a), high magnification (1x1 µm²) b) and phase image (c); unsized CF at low magnification d), high magnification e) and phase image (f); HRBC-CF at low magnification g), high magnification h) and phase image (i); CNT-g-CF at low magnification j), high magnification k) and phase image (l). [Color image]

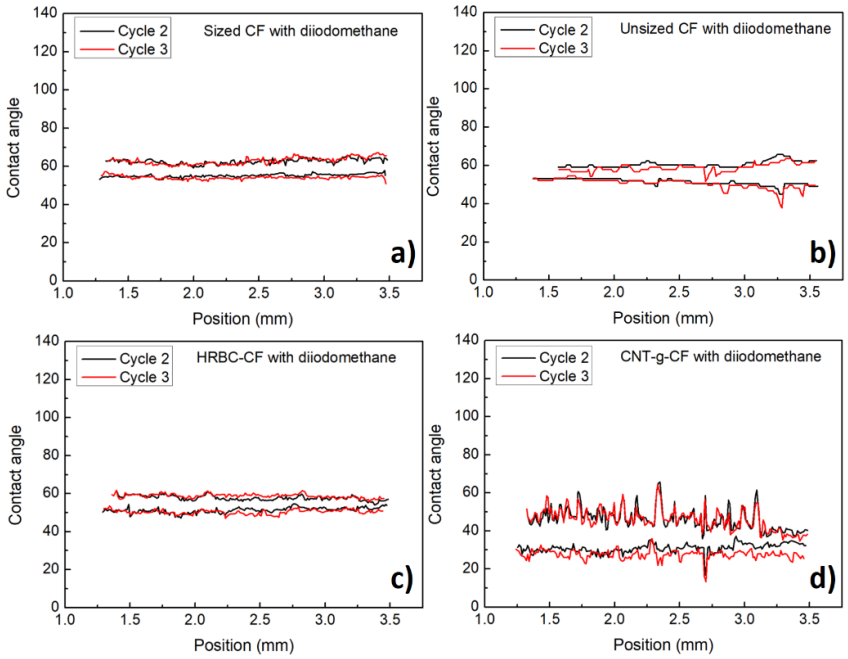


Figure 4: Contact angles determined for fiber samples using the Wilhelmy method, a) sized CF, b) unsized CF, c) HRBC-CF, and d) CNT-g-CF with diiodomethane (DIM) for cycle 2 and 3 shown with black and red lines, respectively. [Color image]

Table 1 Advancing (ϑ_a) and receding (ϑ_r) contact angles presented with standard deviations, equilibrium (ϑ_{equ}) contact angle, and contact angle hysteresis ($\Delta\theta$) for the four fiber samples and ϑ_{equ} calculated using the Wenzel model for individual CNTs with test liquids are presented with associated error.

Test liquid	Sample	θ_a (°)	θ_r (°)	θ_{equ} (°)	$\Delta\theta$ (°)
Deionized water	Sized CFs	83.4 ± 3.0	37.6 ± 5.8	63.1 ± 2.6	45.8
	Unsized CFs	72.0 ± 9.0	35.7 ± 10.1	55.9 ± 6.3	36.3
	HRBC-CFs	95.3 ± 2.9	75.9 ± 3.9	85.6 ± 2.4	19.4
	CNT-g-CFs	99.7 ± 4.2	53.5 ± 7.3	77.7 ± 3.7	46.2
	CNT-g-CFs*	-	-	79.6 ± 3.1	-
Ethylene glycol	Sized CFs	61.2 ± 4.7	25.4 ± 5.7	46.2 ± 3.3	35.8
	Unsized CFs	61.4 ± 11.9	24.8 ± 9.2	46.1 ± 7.7	36.6
	HRBC-CFs	69.8 ± 2.6	43.5 ± 3.5	57.7 ± 2.1	26.3
	CNT-g-CFs	67.0 ± 4.8	28.8 ± 5.4	50.7 ± 3.3	38.2
	CNT-g-CFs*	-	-	57.4 ± 2.6	-
Diiodomethane	Sized CFs	61.3 ± 2.6	54.2 ± 2.0	57.8 ± 1.6	7.1
	Unsized CFs	62.4 ± 4.6	55.0 ± 2.7	58.8 ± 2.7	7.4
	HRBC-CFs	59.5 ± 2.5	52.2 ± 2.2	55.9 ± 1.7	7.3
	CNT-g-CFs	44.7 ± 8.2	30.8 ± 11.7	38.3 ± 6.7	13.9
	CNT-g-CFs*	-	-	48.1 ± 4.7	-

Table 2: Surface energy components of the fiber samples calculated using the acid-base model, with literature values for polypropylene (PP) [7]. Total fiber surface energy (γ), Lifshitz-van der Waals (γ^{LW}) acid-base (γ^{ab}) surface energy components as well as acid (γ^+) and base (γ^-) surface energy parameters, and work of adhesion (W_a) for the fiber samples with PP matrix, presented with associated error, .

Sample/ material	γ (mJ/m²)	γ^{LW} (mJ/m²)	γ^{ab} (mJ/m²)	γ^+ (mJ/m²)	γ^- (mJ/m²)	Condition number	W_a (mJ/m²)
PP	30.87 ± 0.52	29.90 ± 0.47	0.97± 0.20	0.12 ± 0.05	1.97 ± 0.31	-	
Sized CFs	34.87 ± 1.48	29.83 ± 0.95	5.05 ± 1.13	0.62 ± 0.26	10.23 ± 1.54	3.59	64.16 ± 1.52
Unsized CFs	34.98 ± 3.33	29.25 ± 1.55	5.72 ± 2.94	0.56 ± 0.56	14.59 ± 4.09	4.41	63.90 ± 2.00
HRBC-CFs	32.08 ± 1.05	30.92 ± 0.97	1.17 ± 0.41	0.19 ± 0.12	1.75 ± 0.64	3.99	62.96 ± 1.43
CNT-g-CFs	40.71 ± 3.38	40.46 ± 3.27	0.26 ± 0.84	0.01 ± 0.04	2.63 ± 1.20	3.63	70.91 ± 2.66
CNT-g-CFs*	35.61 ± 2.72	35.32 ± 2.61	0.29 ± 0.78	0.01 ± 0.04	3.10 ± 1.11	3.62	66.44 ± 2.41

Table 3: Near-surface chemical composition of fiber samples determined by XPS and the ratios of carbon to oxygen (C/O) for fiber samples determined from XPS.

Sample	Chemical composition						
	C (at.%)	O (at.%)	N (at.%)	Si (at.%)	Fe (at.%)	Ni (at.%)	C/O
Sized CFs	84.07	14.53	0.83	0.57	-	-	5.79
Unsized CFs	81.34	9.96	2.98	5.71	-	-	8.16
HRBC-CFs	84.52	12.38	1.32	1.53	0.13	0.12	6.82
CNT-g-CFs	96.28	3.15	-	-	0.56	-	30.56

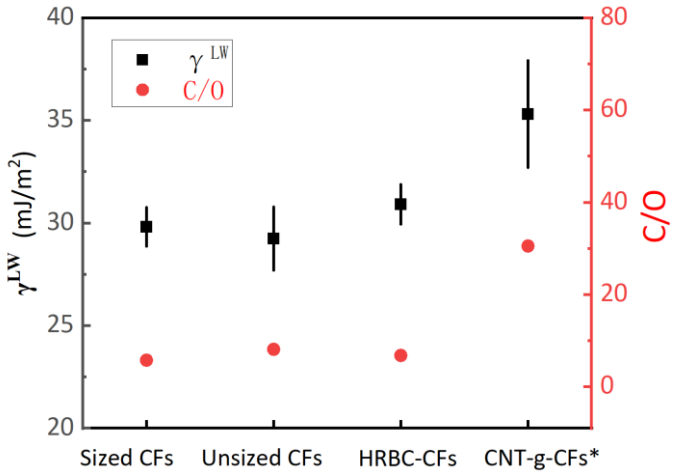


Figure 5: The relationships between γ^{LW} and C/O as a function of four carbon fibers samples.

Table 4: Average interfacial shear strengths (IFSS) determined by single carbon fiber microdroplet tests with a PP matrix with associated standard error. Fiber diameters measured from SEM post fracture.

Sample	IFSS (MPa)	Number of samples tested	Average fiber diameter (µm)
Sized CFs	8.07 ± 0.21	47	7.14 ± 0.17
Unsized CFs	7.30 ± 0.24	33	7.20 ± 0.34
HRBC-CFs	8.03 ± 0.16	50	6.89 ± 0.96
CNT-g-CFs	11.20 ± 0.34	58	7.28 ± 0.36

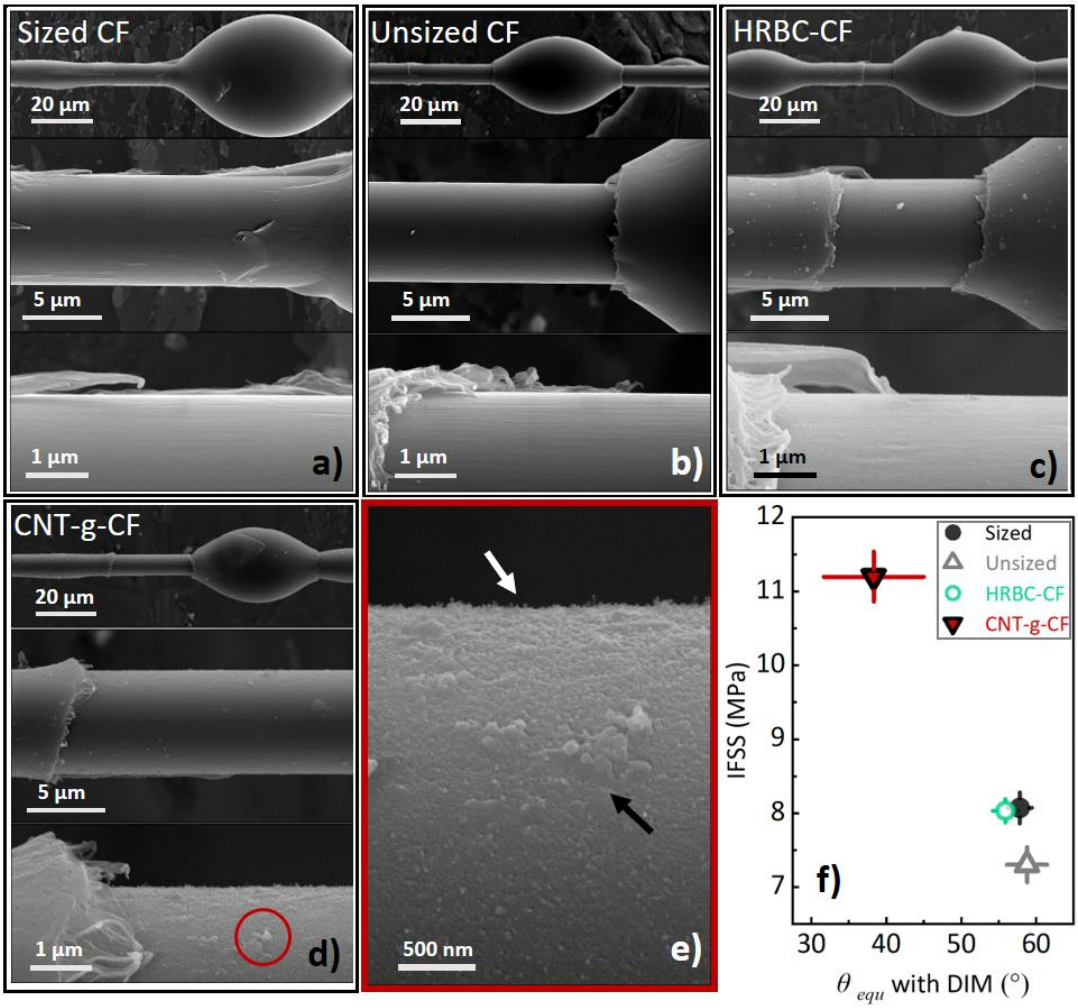


Figure 6: Fractography micrographs of microdroplet fiber-polypropylene model composites, a) sized CF, b) unsized CF, c) HRBC-CF, d) CNT-g-CF, e) CNT-g-CF high magnification of fracture surface circled in d), with residual PP indicated with a black arrow and fractured CNTs indicated by the white arrow. f) Relationship between the equilibrium contact angle of CFs in DIM and the IFSS results from microdroplet PP single fiber composites. [Color image]